Mon. Not. R. Astron. Soc. **000**, 000–000 (0000) Printed 3 May 2002 (MN LaTeX style file v1.4)

X-ray Spectroscopy of the IP PQ Gem

Cynthia H. James, Gavin Ramsay, Mark Cropper and Graziella Branduardi-Raymont
Mullard Space Science Laboratory, University College London, Holmbury St.Mary, Dorking, Surrey, RH5 6NT

3 May 2002

ABSTRACT

Using *RXTE* and *ASCA* data, we investigate the roles played by occultation and absorption in the X-ray spin pulse profile of the Intermediate Polar PQ Gem. From the X-ray light curves and phase-resolved spectroscopy, we find that the intensity variations are due to a combination of varying degrees of absorption and the accretion regions rotating behind the visible face of the white dwarf. These occultation and absorption effects are consistent with those expected from the accretion structures calculated from optical polarisation data. We can reproduce the changes in absorber covering fraction either from geometrical effects, or by considering that the material in the leading edge of the accretion curtain is more finely fragmented than in other parts of the curtain. We determine a white dwarf mass of $\sim$1.2 using the *RXTE* data.

Key words: binaries: close - stars: individual: PQ Gem - stars: magnetic fields - novae, cataclysmic variables - X-rays: stars - accretion

1 INTRODUCTION

Magnetic cataclysmic variables (MCVs) can be split into two groups: those in which the magnetic field of the accreting white dwarf is strong enough ($\gtrsim$ 10MG) to synchronise its spin period with that of the binary orbital period – the polars, and those with a magnetic field insufficiently strong to achieve this synchronisation – the intermediate polars (IPs). The MCV PQ Gem is unusual in that it exhibits characteristics of both groups: it shows a strong soft X-ray component (kT $\sim$50eV) (Duck et al. 1994), it is polarised in the optical/IR wave-bands (Potter et al. 1997; Piirola, Hakala & Coyne 1993) and has an estimated magnetic field strength of $\sim$8–21 MG (Väth, Chanmugam & Frank 1996; Potter et al. 1997; Piirola et al. 1993) – all of which are characteristics of polars. On the other hand it shows a spin period of 833.4 sec (Mason 1997) and an orbital period of 5.19 hrs (Hellier, Ramseyer & Jablonski 1994) which are typical of IPs. PQ Gem can therefore be thought of as the first true "intermediate" polar (Rosen, Mittaz & Hakala 1993).

PQ Gem has been observed using several X-ray satellites (*ROSAT*, *Ginga*, *ASCA* & *RXTE*). The X-ray light curves show a prominent modulation on the spin period, in particular, a pronounced dip in the light curve which is thought to be due to an accretion stream obscuring the main emission region on the surface of the white dwarf. Mason (1997) made a study of the then available X-ray data to determine an accurate ephemeris for PQ Gem based on timings of the dip. However, a detailed study of the spectral information contained in the *ASCA* data was not undertaken.

This paper is primarily targeted at reaching a greater understanding of the interplay between the emission sites and absorption which produces the observed modulation of the X-ray light curves. This is achieved through analysis of the *ASCA* spectral data with supporting evidence from the hard X-ray *RXTE* light curves. The mass of the white dwarf is calculated from the *RXTE* spectral data using the stratified accretion column model of Cropper et al. (1999, subsequently CWRK). A fuller report is available in James (2001).

2 OBSERVATIONS AND DATA REDUCTION

2.1 ASCA

ASCA was launched in 1993 carrying two X-ray CCD cameras (SIS) and two imaging gas scintillation proportional counters (GIS), and operated until 2000 (Tanaka, Inoue & Holt 1994). The SIS detectors covered the energy range of 0.4 keV to 10keV with an energy resolution of 2% at 5.9 keV. The GIS detectors had an energy range of 0.7 keV to 10 keV with energy resolution of 8% at 5.9 keV. Above 8keV the GIS had a greater effective area than the SIS.

Details of the observations of PQ Gem are given in Table 1. The SIS detectors were configured to faint data mode 2-CCD (high bit rate) and 1-CCD (medium bit rate) clocking modes and the GIS detectors were configured to PH-mode. It is not possible to merge data from the different types of detector or from different SIS clocking modes with-

Date	Instrument	Bit rate	Integration time (s)	Average cts/s
1994/11/04	SIS0	high	26786	0.35
		medium	36910	0.38
	SIS1	high	24732	0.29
		medium	34734	0.31
	GIS2	high	27771	0.25

Table 1. Details of the *ASCA* observations and data used in the analysis for this paper.

Date	Instrument	Integration time (s)	Average cts/s
1997/01/27-30	PCA	51216	13.9

Table 2. Details of the *RXTE* PCA observations and data used in the analysis for this paper.

out loss of information. Hence the end product of the data selection and reduction was several data files with effective exposures ranging from 24.7–36.9ksec.

The data selection and reduction were carried out following recommended procedures (details in James 2001). The observation was made early in the *ASCA* mission prior to the onset of the degradation of the CCDs due to radiation damage (Yaqoob et al. 2000). Hence, the background spectra for SIS were created using the appropriate blank-sky event lists (available as part of *ASCA* calibration data) together with the data selection criteria corresponding to each event list. Background spectra for GIS were created in a similar fashion using blank-sky event lists. Background light curves were created from a source-free region of the same observation and subjected to the same screening criteria as for the source light curves.

2.2 RXTE

The Rossi X-ray Timing Explorer (*RXTE*) was launched on 30th December, 1995. A review of the available instrumentation and the scientific results of the first years are given in Swank (1998).

Details of the *RXTE* observations of PQ Gem used in this paper are given in Table 2. Only the top Xenon layer was selected from the five PCA instruments, so as to improve the signal-to-noise ratio. The standard *RXTE* procedures were used to select data (details in James 2001). The background was modelled using the latest faint background model appropriate for the epoch of the observation, *i.e.* files faintl7_e03v03.mdl and faint240_e03v03.mdl.

3 LIGHT CURVES

The quadratic spin ephemeris of Mason (1997) was used throughout the analysis of the light curves which were heliocentrically corrected.

3.1 Period Analysis

The variability in the *RXTE* and *ASCA* light curves was analysed using a standard discrete Fourier transform (DFT) code (Deeming 1975, Kurtz 1985). The equation, $z_0 = -ln[1-(1-p_0)^{1/N}]$, (Scargle 1982) was used to determine the power level, z_0, above which an amplitude peak would be spurious for a small fraction, p_0, of the time, where N is the number of frequencies examined. A 90% confidence ($p_0 = 0.1$) was used to determine the signal-to-noise level above which the amplitude of a power peak was judged to be significant. The noise level of the periodogram was taken to be the mean of the amplitude spectrum after it had been prewhitened with frequencies found to be significant (Table 3). The error in each such frequency was taken to be the standard deviation, σ, from a least squares fitting.

The *ASCA* data showed three significant periods, 833.46s, 416.678s and 277.763s which are consistent with spin ephemeris of Mason (1997) and its first two harmonics. The *RXTE* data showed a significant period of 833.54s. The spin period (833 sec) is consistent with the spin down rate predicted by the ephemeris of Mason (1997). The complete results are given in Table 3 for those signals identified as significant at the 90 percent confidence level. The amplitude spectra, and window functions for the *RXTE* and *ASCA* are shown in Figure 1, along with the spectra prewhitened with the frequencies of the significant power peaks and the expected positions of the orbital, beat, spin frequencies and spin harmonics. The residual power peaks in the prewhitened *RXTE* periodogram are the 3rd harmonic of the spin period (> 68% confidence level) and the 1st and 2nd harmonics (<68% confidence level).

Using an orbital period of 5.19hrs (Hellier et al. 1994) a beat period at 14.54 min may be expected. However, there is no evidence for a significant amplitude at the frequencies corresponding to the orbital or beat periods in either the *RXTE* or the *ASCA* data (Figure 1). This indicates that the accreting material must go through a disc since all orbital information will then be lost.

3.2 ASCA light curves

Light curves of these data were first presented in Mason (1997) and also in James et al. (1998). They are presented here for completeness and comparison with those from *RXTE*. Light curves using data from the SIS0 detector for energy bands 0.7–1.0keV, 1.0–2.0keV and 2.0–4.0keV, 4.0–10.0keV and from the total bandpass (0.7–10.0keV) folded on spin period are shown on the left-hand side of Figure 2. The light curves were not folded on either the orbital or beat periods due to the lack of amplitude peaks found at these frequencies in the power spectrum of the *ASCA* data (§3.1).

3.3 RXTE light curves

Light curves were extracted for the energy bands 2.0–4.0keV, 4.0–10.0keV, 8.0–25.0keV and from the total bandpass, 2.0–25keV, which were then folded on the spin period (right-hand side, Figure 2). The first two energy bands can be directly compared with similar plots using the *ASCA* data.

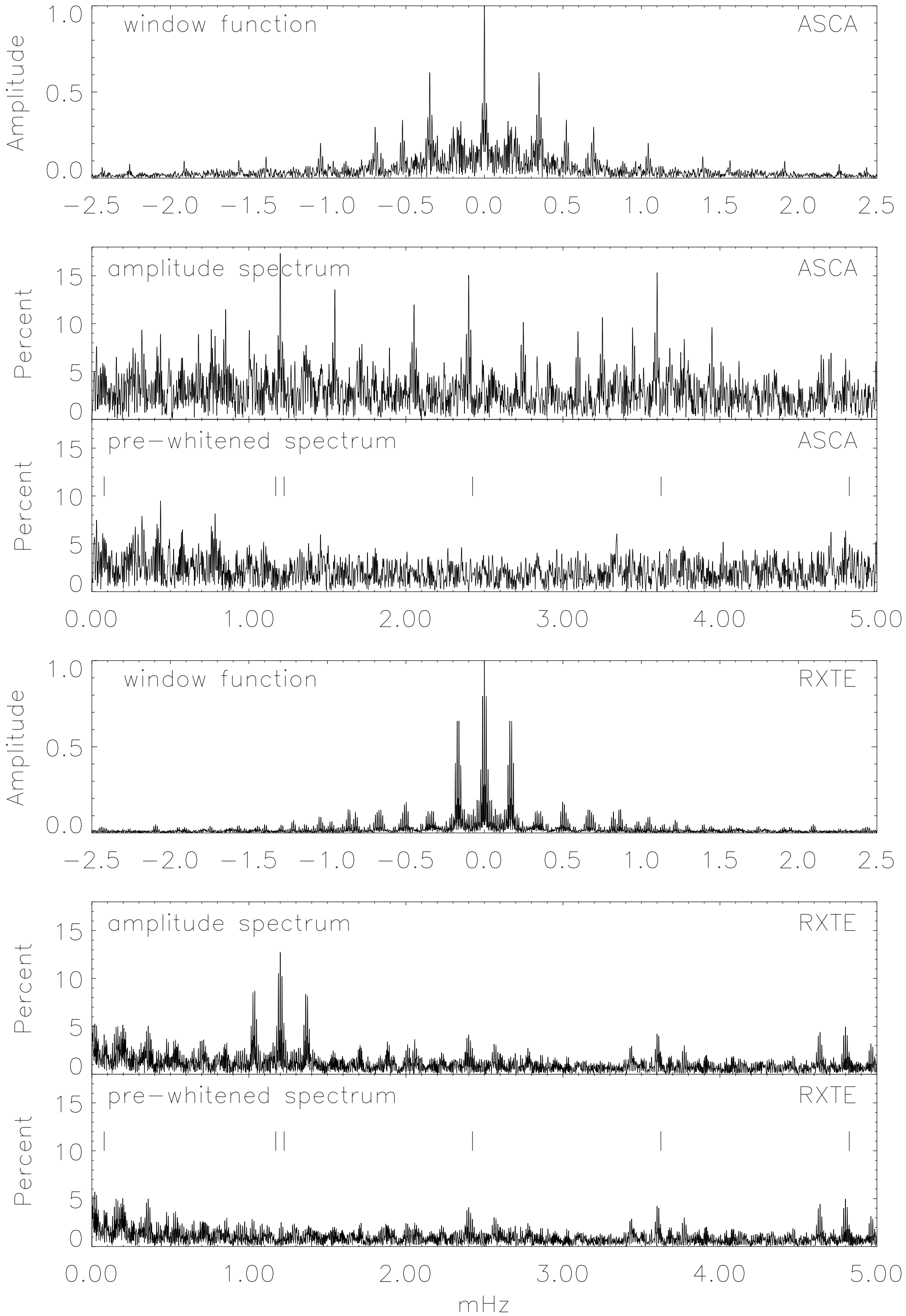

Figure 1. Periodograms for the *ASCA* 0.5–10.0keV light curve (upper half) and *RXTE* 2.0–25.0keV light curve (lower half) of PQ Gem. In each half the top plot shows the window function, in the middle plot, the amplitude spectrum, and the bottom plot shows the spectrum prewhitened with the frequencies of the significant peaks. The vertical bars (from left to right) mark the position of the orbital, beat and spin (ω) frequencies plus the 1st, 2nd and 3rd harmonics of ω, respectively. The relevant details are given in §3.1 and Table 3.

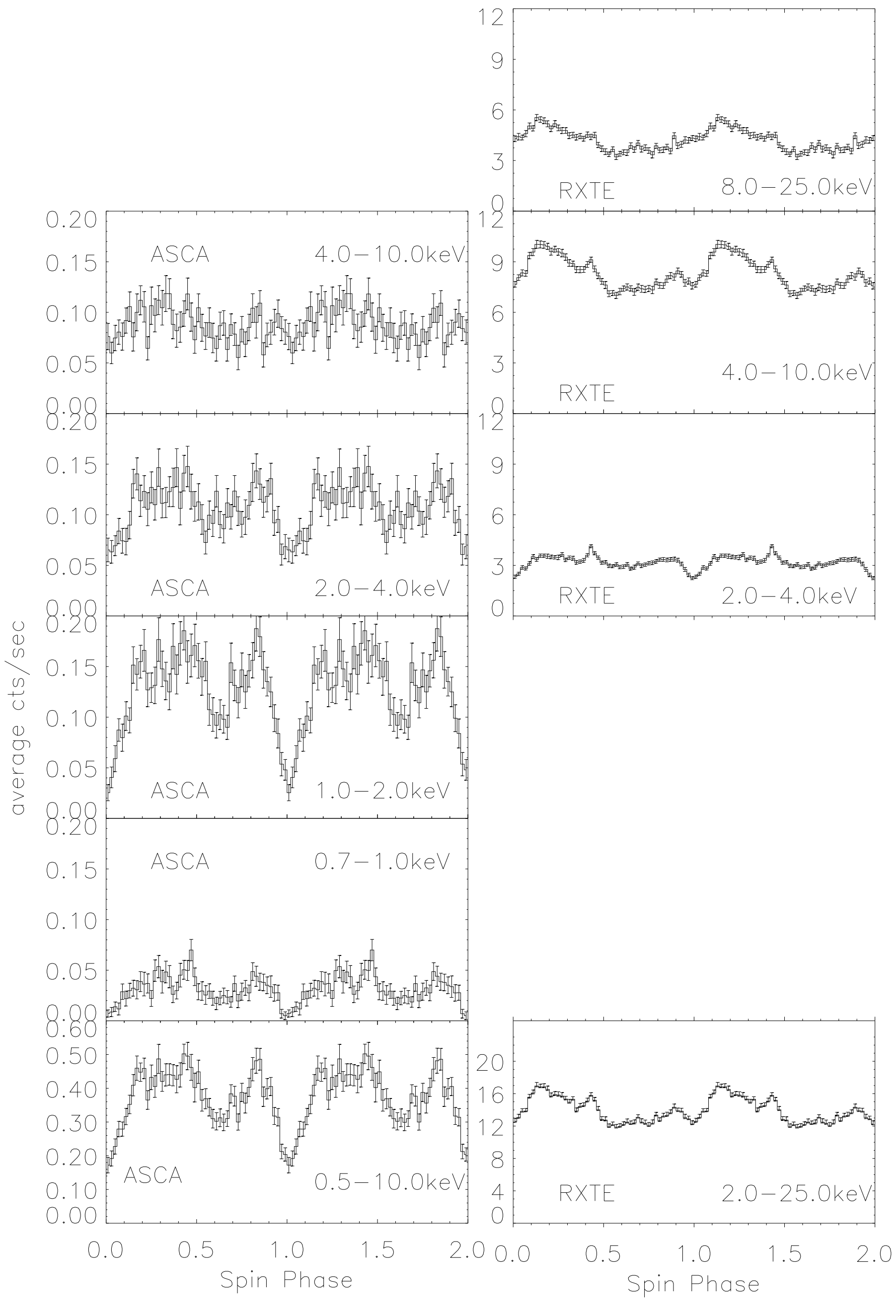

Figure 2. Background-subtracted light curves of PQ Gem using *ASCA* SIS0 and *RXTE* PCA data folded on the spin period. On the left hand side are the *ASCA* light curves for energy bandwidths 4.0–10keV (top), 2.0–4.0keV (second from top), 1.0–2.0 keV (middle) and 0.7–1.0keV (second from bottom) 0.5–10.0keV (bottom). On the right hand side are the *RXTE* light curves for energy bandwidths 8.0-25.0keV (top), 4.0-10.0keV (second to top), 2.0-4.0keV (third to top), 2.0-25keV (bottom).

3.4 Comparison between the ASCA and RXTE light curves

The *RXTE* PCA instrument overlaps the *ASCA* SIS instruments across the 2–10keV energy band. Hence this energy band from both instruments was used to compare the light curve modulation of the two observations (Figure 2). The light curves in these 2 bandpasses were found to be very similar, each with two maxima separated by a minimum at spin phase $\phi \sim 0.0$ (referred to as "the dip", Mason et al. 1992) and a second minimum at $\phi \sim 0.6$. In the 4.0–10.0keV light curves the minima are relatively shallow in both the *ASCA* and the *RXTE* light curves, but the 2.0-4.0keV light curves show well defined "dips" at $\phi = 0.0$, with a broader minimum at $\phi \sim 0.6$. There is some evidence that the amplitude

Satellite	Instrument	Passband keV	Frequency mHz	Period s	S/N
ASCA	SIS1	0.7-10.0	1.19981(25)	833.46(17)	8.0
			2.39994(32)	416.678(56)	7.1
			3.60019(32)	277.763(25)	6.6
RXTE	PCA	2.0-25.0	1.199703(81)	833.540(56)	12.8

Table 3. The details of the significant power peaks found from period analysis of *ASCA* SIS1 data and *RXTE* PCA data. The signal-to-noise ratio was taken as the amplitude of power peak to the mean of the prewhitened spectrum.

of the variation in the *RXTE* folded light curve is less than that in the *ASCA* SIS data. The shape of "the dip" in the 2.0-4.0keV band is "V"-shaped in the *RXTE* compared to a more "U"-shaped in the *ASCA* light curve and its depth appears greater in the latter. This may be due to a higher level of absorption at the earlier epoch of the *ASCA* observation.

3.5 RXTE hardness ratios

Plots of the 8.0–25.0keV/2.0–8.0keV and 8.0–25.0keV/2.0–4.0keV hardness over the spin period are shown in Figure 3. The lower limit of the 8.0–25.0keV energy band was chosen so as to be well above the main absorption edges. A higher value of the ratio indicates those positions in the spin cycle which are more affected by absorption. These are consistent with the dip at $\phi = 0.0$ being due to absorption.

4 SPECTRAL ANALYSIS

Because the energy resolution of the *RXTE* PCA (18% at 6.0keV) is much poorer than that of the *ASCA* SIS (2%), and does not extend to lower energies, the spectral analysis was restricted to the *ASCA* data. During the spectral analysis the medium and high bit rate SIS data from both instruments and the GIS data were linked through the models and fitted simultaneously.

4.1 Integrated Spectrum

The integrated spectrum was modelled using the MEKAL code for an optically thin emission model (Mewe, Kaastra & Liedahl 1995) for the hard X-ray spectrum and a blackbody model for the soft X-ray continuum. The temperature of the former was difficult to constrain, a problem which was similarly experienced by Duck et al. (1994) using *Ginga* data. Therefore the temperature was fixed at 20keV in line with the results from their analysis (we tried fixing the temperature at other values, but this did not have a significant effect on the results). The temperature of the blackbody component was not well constrained and therefore this spectral component was fixed at 55eV in line with that found with *ROSAT* data (Duck et al. 1994) due to its greater sensitivity to this spectral range. The fluorescent iron line at 6.4keV was modelled using a Gaussian component, the width of which was fixed at 0.05keV. A single homogeneous photo-electric absorber gave a poor fit ($\chi^2_\nu = 2.0$), therefore an inhomogeneous (partial covering) photoelectric absorber was added to the model. A good fit to the data was achieved in this way

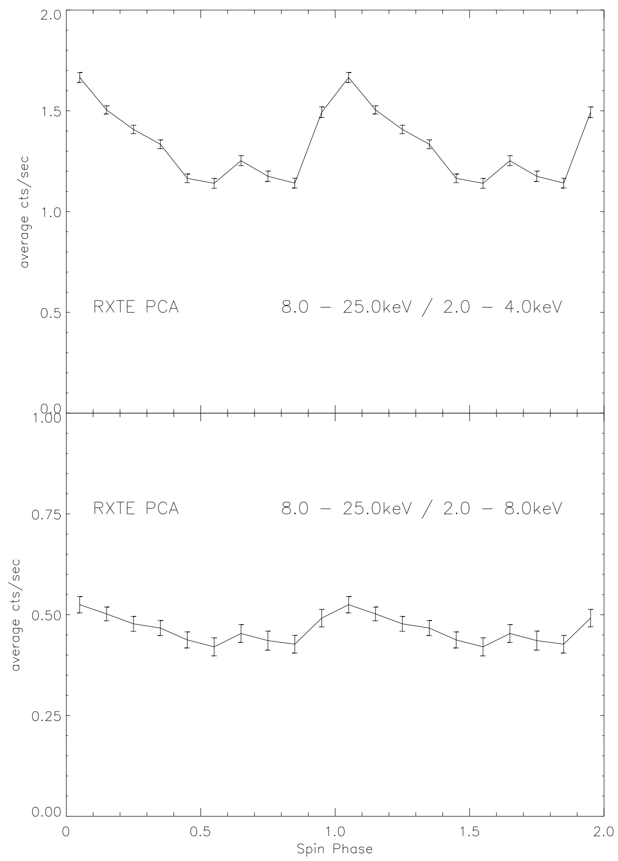

Figure 3. Plots of the 8.0–25.0keV/2.0–8.0keV (below) and 8.0–25.0keV/2.0–4.0keV (above) hardness ratios folded on the spin period. The errors are 1σ.

($\chi^2_\nu = 1.07$). The values of those parameters allowed to vary during the fitting are given in Table 4 and the integrated spectra are plotted in Figure 4.

4.2 Phase-resolved Spectroscopy

Even though a good fit to the integrated spectrum was obtained, the results from the 8.0–25.0keV/2.0–8.0keV and 8.0–25.0keV/2.0–4.0keV hardness ratios using the *RXTE* PCA data indicate the possibility of variation in the absorption during the spin cycle (Figure 3, §3.5). These two results imply that variability in both the absorption and the normalisation of the hard X-rays over the spin cycle could be the cause of the observed modulation in the spin-folded light curves. In order to investigate this further we divided

$N_H(1)$ 10^{22} cm^{-2}	$N_H(2)$ (fraction) 10^{22} cm^{-2}	BB norm: 10^{-3}	MEKAL norm: 10^{-2}	Gaussian norm: 10^{-5}	Flux(observed) 2-10keV 10^{-11}erg cm^{-2} s^{-1}	χ^2_ν (dof)
$0.12^{+0.02}_{-0.03}$	$8.3^{+0.9}_{-1.3}$ $(0.53^{+0.01}_{-0.02})$	$2.0^{+2.3}_{-0.4}$	$1.71^{+0.05}_{-0.06}$	$4.9^{+1.3}_{-0.9}$	2.12	1.07 (1070)

Table 4. Results from spectral analysis of the *ASCA* integrated spectrum of PQ Gem including the error range at 90% confidence level. The optically thin plasma and blackbody temperatures were fixed at 20keV and 55eV respectively. $N_H(1)$ corresponds to the homogeneous absorber whereas $N_H(2)$ applies to the inhomogeneous (partial covering) absorber; the flux is not corrected for absorption. The model was fitted simultaneously to the medium and high bit rate data from the SIS1 and SIS0 instruments and the high bit rate data from the GIS2 instrument.

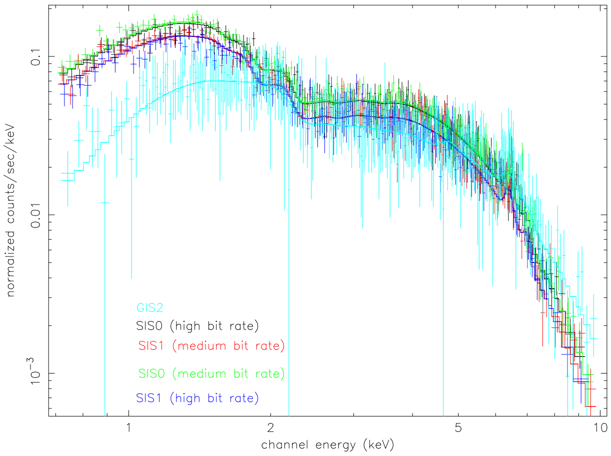

Figure 4. Integrated spectra of PQ Gem. Data from the medium and high bit rate data from the SIS1 and SIS0 instruments and the high bit rate data from the GIS2 instrument with the fitted model (Table 4).

the spin period into 10 equal time bins and extracted spectra for each using data from both the SIS and GIS2 instruments. During all subsequent spectral fitting the medium and high bit rate data from both SIS and the GIS2 instruments were linked through the models and fitted simultaneously.

The reference model was derived from $0.4 \le \phi < 0.5$, since this phase had the greatest number of counts. The model resembled that obtained from the integrated spectrum with the exception of the blackbody component whose temperature was significantly higher (best fit=83eV). In this more detailed analysis it was considered to be more appropriate to fix the temperature of the blackbody component of the other phase resolved spectra at this value. The best fit model comprised of three emission components: an optically thin plasma emission component with a temperature of 20keV (fixed), a blackbody component with a temperature of 83eV and a Gaussian at 6.4keV to model the fluorescent Fe emission line (fixed width of 0.05keV). Two photoelectric absorption components were required to model the attenuation of the X-rays: an inhomogeneous (partial covering) neutral absorber and a homogeneous neutral absorber. The latter had a best fit of 6.8×10^{20} cm^{-2}: this component was fixed at this value in the other phase intervals. The metal abundance had a best fit of 0.34 solar - again this was fixed at other phase intervals. We now allowed the normalisation of the X-ray emission and the partial covering absorption component to vary during the remaining 9 phase bins of the *ASCA* data. We also allowed the normalisation of the blackbody and the Fe fluorescent emission line to vary.

The resulting best fit parameter values from this analysis are shown in Table 5. The variations in the normalisation of the optically thin plasma, the column density and partial covering fraction are plotted in Figure 5, together with the folded light curve for the 0.5–10.0keV energy band of the *ASCA* data. It can be seen that the column density does not vary significantly over the whole spin cycle. The normalisation parameter of the hard X-ray component shows a maximum over $0.2 \le \phi < 0.4$, decreasing to a minimum at $\phi = 0.7$. The covering fraction of the partial absorber component shows a steady decline from its maximum value at $\phi = 0.0$ to a minimum value at $\phi = 0.5$. This pattern and phasing closely follows that of the *RXTE* 8.0–25.0keV/2.0–8.0keV hardness ratio, shown in Figure 3.

Relating this back to the main features of the modulation of the light curve shows that the maximum countrate $(0.1 \le \phi < 0.4)$ is due to a combination of increasing normalisation coupled with a decreasing level of absorption. It would appear that an increase in the normalisation factor is probably the main cause of the second maximum (0.75 $\le \phi <$ 0.85) of the light curve, but a contribution from a decrease in the covering fraction may also play a part. The secondary minimum $(0.55 \le \phi < 0.75)$ is mainly due to a lower normalisation factor. Finally, “the dip” can be accounted for by the maximum value of the covering fraction, although, again, a contribution from a slight decrease in the normalisation factor cannot be ruled out.

5 MASS OF THE WHITE DWARF

5.1 Procedure

In recent years much work has been done in determining the shock temperature in magnetic CVs (e.g. Cropper, Ramsay & Wu 1998, Fuijmoto & Ishia 1996). One of the main goals of this work has been to estimate the mass of the white dwarf since these two parameters are closely linked. To estimate the mass of the white dwarf in PQ Gem we use the emission model of Cropper et al. (1999) (CWRK) to fit data from the RXTE PCA detector (since it has an extended high energy range - the temperature of the hard X-ray component was poorly constrained using the ASCA data because of the 10keV upper limit). This model was developed to fit high quality X-ray spectra appropriate to the conditions found in the accretion sites of MCVs. It is a more complex model than the generalised optical thin plasma code we used for the phase-resolved spectroscopy.

Spin Phase	$N_H(2)$ 10^{22} cm^{-2}	Covering Fraction	BB Norm: 10^{-4}	MEKAL Norm: 10^{-2}	Gaussian: Norm: 10^{-5}	Flux(observed) 2–10keV 10^{-11}erg cm^{-2} s^{-1}	χ^2_ν (dof)
0.0-0.1	$7.4^{+1.5}_{-1.5}$	$0.80^{+0.02}_{-0.02}$	$0.48^{+1.03}_{-0.48}$	$1.88^{+0.21}_{-0.18}$	$7.96^{+2.94}_{-6.33}$	1.86	1.09 (149)
0.1-0.2	$8.6^{+2.4}_{-2.2}$	$0.70^{+0.03}_{-0.04}$	$1.62^{+0.57}_{-1.60}$	$2.10^{+0.26}_{-0.22}$	$11.9^{+3.20}_{-5.64}$	2.17	1.00 (198)
0.2-0.3	$5.4^{+2.5}_{-1.3}$	$0.59^{+0.03}_{-0.03}$	$1.24^{+0.51}_{-0.54}$	$2.22^{+0.20}_{-0.16}$	$12.7^{+3.20}_{-5.69}$	2.59	1.11 (248)
0.3-0.4	$5.7^{+2.2}_{-1.5}$	$0.55^{+0.03}_{-0.04}$	$1.63^{+0.45}_{-0.64}$	$2.21^{+0.21}_{-0.17}$	$7.77^{+4.53}_{-4.21}$	2.55	0.91 (245)
0.4-0.5	$8.1^{+3.9}_{-2.7}$	$0.47^{+0.06}_{-0.05}$	$1.16^{+0.55}_{-0.38}$	$2.18^{+0.28}_{-0.20}$	$8.00^{+3.50}_{-5.09}$	2.49	1.12 (253)
0.5-0.6	$3.8^{+2.0}_{-1.5}$	$0.43^{+0.04}_{+0.04}$	$1.47^{+0.55}_{-0.43}$	$1.79^{+0.17}_{-0.14}$	$7.02^{+2.68}_{-5.94}$	2.23	1.08 (241)
0.6-0.7	$6.9^{+4.1}_{-2.6}$	$0.54^{+0.05}_{-0.06}$	$0.58^{+0.48}_{-0.35}$	$1.69^{+0.23}_{-0.17}$	$11.7^{+3.30}_{-5.42}$	1.96	0.98 (202)
0.7-0.8	$4.0^{+1.9}_{-1.3}$	$0.52^{+0.03}_{-0.04}$	$0.65^{+0.49}_{-0.36}$	$1.61^{+0.13}_{-0.12}$	$6.69^{+3.51}_{-3.89}$	1.96	0.99 (209)
0.8-0.9	$8.1^{+3.9}_{-2.7}$	$0.50^{+0.05}_{-0.05}$	$0.52^{+0.47}_{-0.46}$	$1.99^{+0.20}_{-0.18}$	$4.21^{+3.98}_{-4.06}$	2.23	1.04 (231)
0.9-0.0	$4.8^{+1.5}_{-1.1}$	$0.58^{+0.03}_{-0.03}$	$1.42^{+0.48}_{-0.55}$	$1.87^{+0.16}_{-0.12}$	$11.8^{+3.20}_{-5.24}$	2.2	0.95 (218)

Table 5. The variable parameter values from spin phase-resolved spectral analysis over 10 phase-bins. The reference model ($0.4 \leq \phi <$ 0.5) was simultaneously fitted to the medium and high bit rate data from both of the SIS instruments and high bit rate data from the GIS2 instrument on the *ASCA* satellite.The normalisation and absorption parameters only were varied from those of the reference model. The blackbody, bremssstralung normalisations and absorption include the error range at the 90% confidence level. The blackbody, Mekal and Gaussian normalisations are standard for the relevant *xspec* models. Also included are the χ^2_ν and observed flux (i.e. not corrected for absorption) for the 10 phases.

The parameter, ϵ_s (the ratio of the cyclotron to bremsstralung cooling at the shock), was fixed at 0.5 which, from figure 1b of Wu, Chanmugam & Shaviv (1995) corresponds to a magnetic field strength of $\sim$ 15MG (Piirola et al. 1993, Väth et al. 1996, Potter et al. 1997). We stratified the volume between the surface of the white dwarf and the shock front (Cropper et al. 1998) into 100 levels. The free parameters during the spectral fitting were the specific accretion rate in g cm^{-2}s^{-1}, and the mass of the white dwarf. A viewing angle is also required to scale the reflection component in the model. The abundance was allowed to vary from a solar profile in the final stages of the fitting.

5.2 The Results

The *RXTE* spectral fitting was restricted to the spin phase range of the data to $0.1 \leq \phi < 0.5$ which corresponds to that portion of the spin cycle where a single emission site is visible (Potter et al. 1997). This phase range also excludes the dip centered on ϕ =0.0 which from *ROSAT* and *ASCA* data, has been shown to be due to absorption. Models including a homogeneous absorber components together with a CWRK emission component were found to be sufficient to produce an acceptable fit (χ^2_ν ~0.89) to this data using an estimated average viewing angle of ~60°. This gave a white dwarf mass of 1.21M$_\odot$ (Table 6). We discuss this further in §6.6.

6 DISCUSSION

In section 4.2 we find that the spin phase modulation can be modelled well by a variation in the partial covering fraction of a neutral absorber at low energies and in the normalisation at higher energies. Before we discuss this further, we briefly examine whether the modulation at both high and low energies can both be explained by a tall accretion shock.

In the case where the shock has significant vertical extent, the lower (cooler) part of the shock could be obscured by the limb of the white dwarf at certain spin phases. The light curves will then have a larger amplitude at low energies than at high energies (e.g. Allan, Hellier & Beardmore 1998). The height of the accretion column, H, can be estimated from the relationship

$$H = 5.45 \times 10^8 \dot{M}_{16}^{-1} f_{-2} M_{WD}^{3/2} R_{WD}^{1/2}$$

(Frank, King & Raine 1991). Using the lower limit of the fractional area and the corresponding $\dot{M}$ derived in §6.4 (cf Table 7) gives an upper bound of H=5.4×10^{7}cm or 0.14 R$_{WD}$. However, the observational evidence suggests that PQ Gem has a significant magnetic field (§1) which implies that the shock height will be lower than this (e.g. Cropper et al. 1999) due to cyclotron cooling. This suggests that this mechanism is not the cause of the variation. However, the accretion regions are likely to be sufficiently structured (e.g. Potter et al 1997) so that such a scenario cannot be excluded. On the other hand, because the spectral variations can be well modelled by a variation in covering fraction and

Satellite	detector	angle $^\circ$	$N_{H,cold}(1)$ 10^{22} cm^{-2}	$\dot{m}$ gcm^{-2}s^{-1}	rc 10^7cm	WD mass $M_\odot$	χ^2_ν (dof)
RXTE	PCA	∼60	5.2	2.3	9.5	1.21 (1.16-1.28)	0.89 (46)

Table 6. Results from fitting the CWRK model to the *RXTE* PCA spectrum ($0.1 \leq \phi < 0.5$).Details of the spectral fitting process are given in §5

$\dot{m}$ (g cm^{-2}s^{-1})	WD mass ($M_\odot$)	χ^2_ν (dof)	unabsorbed flux (0.001-100.0keV) (ergs cm^{-2} s^{-1})	luminosity (ergs s^{-1})	$\dot{M}$ (g s^{-1})	fractional area
0.5	1.20(1.13-1.26)	0.91(52)	6.3×10^{-11}	1.2×10^{32}	3.0×10^{15}	3.1×10^{-3}
1.0	1.21(1.16-1.24)	0.89(52)	6.4×10^{-11}	1.2×10^{33}	2.9×10^{15}	1.6×10^{-3}
5.0	1.22(1.15-1.29)	0.86(52)	6.6×10^{-11}	1.3×10^{33}	2.8×10^{15}	3.4×10^{-4}

Table 7. The effect fixing $\dot{m}$ to a range of values in the CWRK model during the spectral fitting. Details are given in §6.4.

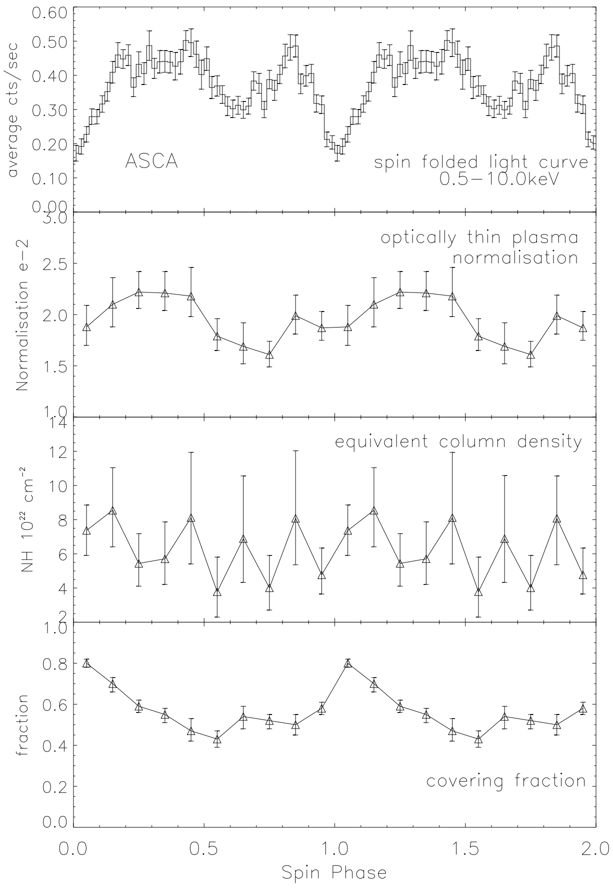

Figure 5. Results from spin phased-resolved spectroscopy of *ASCA* data. $0.4 \leq \phi < 0.5$ is the reference spin phase. The plots from the top are the spin folded light curve (included for clarity), the variation in the hard X-ray normalisation, the column density of the partial covering absorber and its covering fraction.

normalisation, we go on to consider this explanation in more detail.

6.1 Spin Pulse Modulation at Higher Energies

It is evident from an inspection of the 8–25 keV spin-phased *RXTE* light curve (Figure 2) and the spin-phased normalisation in the *ASCA* spectroscopy (Figure 5) that they are broadly similar. As this emission is expected to be at most weakly beamed, this indicates that the variation in intensity is caused by changes in visibility of the X-ray emitting region as the white dwarf rotates. The phase of maximum emission therefore corresponds to the phase of maximum visibility of the emitting region. There is possibly a slight phase shift between the two curves, with a clear peak at $\phi = 0.2$ in the *RXTE* light curve, and a more extended maximum around $0.2 \leq \phi < 0.4$ in the *ASCA* normalisation, but it is unclear given the uncertainties in the normalisations whether this is significant. Spin phases 0.2–0.4 also correspond to the phases at which the accretion region in the upper hemisphere is seen most close to face on (Potter et al 1997, figure 9). This suggests that this is principle cause of the spin pulse modulation at higher energies.

6.2 Spin Pulse Modulation at Lower Energies

At lower energies, the maximum in the covering fraction of the absorber at $\phi = 0.0$ is the major effect on the soft X-ray light curve, while the local increase at $\phi = 0.6$ combined with the decrease in normalisation at this phase to cause the second minimum (§4.2). Potter et al. (1997) find that accretion occurs preferentially along field lines which thread the disc ahead of the accreting pole (their figure 12). Material accreting along these field lines can therefore be identified as the source of the absorption at phase 0.0. Similarly, at $\phi = 0.6$, in the absence of absorption by the disc (cf §6.4), the local increase in covering fraction is likely to be caused by absorbing material along field lines which intersect the line of sight to the lower pole (Potter et al. 1997, figure 9).

Figure 5 indicates that the change in absorption can be explained *entirely* by a change in covering fraction, with the column density of the absorber remaining constant. With reference to figure 9 of Potter et al. (1997), at $\phi = 0.0$, all of the field lines between the disc and the accreting pole will intersect the line of sight. At $\phi = 0.2$, those field lines to the leading part of the accretion region will no longer intersect the line of sight, while by $\phi = 0.4$, only field lines to the trailing part of the accretion region will do so. If the column density through accreting field lines is $\sim 5 \times 10^{22}$ cm^2, the observed variation in covering fraction in Figure 5 can be reproduced.

The accretion flow may be more finely fragmented along field lines feeding the leading edge of the accretion region. This would be expected because finely fragmented material is threaded by the magnetic field more easily than the larger denser inhomogeneities (e.g. Wickramasinghe 1988). From considerations of the packing fraction, the line of sight through more finely fragmented material is less likely to pass between gaps in the flow than in the case of the larger inhomogeneities. This effect would reproduce the high covering fraction at $\phi = 0.0$, and its subsequent decrease towards $\phi = 0.5$.

6.3 Accretion Model

The accretion scenario we are proposing fits neither the standard occultation model of King & Shaviv (1984) nor the accretion curtain model of Rosen, Mason & Córdova (1988). The orientation of the accretion region at spin phase maximum is as predicted by the occultation model, but with absorption effects modifying the light curve significantly. In this it is similar to the "weak field/fast rotator" model of Norton et al. (1999) with the symmetry of the accretion curtain about the magnetic axis modified by the leading field lines preferentially stripping material from the inner margin of the disc. The high (among IPs) magnetic field in PQ Gem and relatively high inclination and low dipole offset ($\sim 60°$ and $\sim 30°$, Potter et al. 1997) ensure that material on accreting field lines travels far enough out of the orbital plane to pass through the line of sight to the accretion region, causing the observed absorption effects. In this it differs substantially from EX Hya which possesses a magnetic field $<$ 1MG.

6.4 Occultation by the Accretion Disc?

Finally, we check whether the accretion disk can extend close enough to the white dwarf for it to have an affect on the X-ray light curves by obscuring the lower emission region.

Using the Ghosh & Lamb formulation (Li, Wickramasinghe & Rudiger 1996) the radius to the truncated inner edge of the accretion disc, r_A, is given by

$$r_A = 0.52\mu_{WD}^{4/7}(2GM)^{-1/7}\dot{M}^{-2/7}$$

where μ_{WD} is the magnetic moment of the white dwarf.

The magnetic moment can be estimated from the relationship $B = \mu/r^3$. Using the fits to the *RXTE* data and the model of CWRK we found a best fit to the white dwarf radius, R_{WD}, of 3.8×10^8 cm. Hence, with a magnetic field strength, B_{WD}, of 15MG (Piirola et al. 1993, Väth et al. 1996, Potter et al. 1997), $\mu_{WD} = 9.6 \times 10^{32}$ G cm^3. The accretion luminosity,

$$L_{acc} = GM\dot{M}/R_{WD}$$

where M is the mass of the white dwarf and L_{acc} is emitted mostly in the X-ray energy band, enables estimation of the accretion rate, $\dot{M}$.

The unabsorbed spectral model from the analysis of the integrated spectrum (§4.1) extrapolated for the energy range 0.001–100.0keV gives the X-ray flux at 3.1×10^{-10}erg cm^{-2} s^{-1} which, taking the distance to PQ Gem of 400pc (Patterson 1994), gives a luminosity of 6.0×10^{33}erg s^{-1} and hence a mass transfer rate rate, $\dot{M}$, of 1.4×10^{16}g s^{-1}. This is typical for IPs (Warner 1995). The resulting $r_A = 1.3 \times 10^{10}$ cm or $\sim 34R_{WD}$ may be too large given that an estimate of the distance to the first Lagrangian point is ≈ 200 R$_{WD}$ (Plavec & Kratochvil 1964) (the main uncertainty in r_A is in the magnetic moment μ_{WD}). Nevertheless it does indicate that with a system inclination of 60° (Potter et al. 1997), the line of sight to the white dwarf surface is likely to be clear of the accretion disc at all spin phases, and this is unlikely to contribute to the cause of the covering fraction variation.

6.5 The size of the Accretion Region

Using the radius of the white dwarf, the specific mass accretion rate, $\dot{m}$, (2.3 g cm^{-2}s^{-1} cf Table 6) and $\dot{M}$ determined above we can derive a fractional accretion area, f, of 9.0×10^{-3}. This is within the normal expectation of $0.001 \lesssim f \lesssim 0.02$ for an IP (Rosen 1992). However, from the *RXTE* data $\dot{M} = 2.9 \times 10^{15}$ g s^{-1} which implies a fractional area of only 7.1×10^{-4}. Refitting the *RXTE* data to the model in which $\dot{m}$ was fixed at 0.5, 1.0 and 5.0 g cm^2 did not give a significant adverse effect on the fit (χ^2_ν=0.91, 0.89, 0.86, respectively). Table 7 gives the implied fractional area and $\dot{M}$ for these $\dot{m}$ as well as the results from the spectral fitting. For a low specific mass accretion rate we find that the implied fractional area is consistent with the lower limit determined using previous observations.

6.6 The Mass of the White Dwarf

Previous determinations of the mass of the white dwarf in PQ Gem using an emission model fitted to *Ginga* data (Cropper et al. 1998, 1999) gave estimates $\geq 1.1\ M_\odot$. In the case of the IP XY Ari, Ramsay et al. (1998) found that there was a good correspondence between the estimates given by this model and those from eclipse mapping. In our work it is found that the *RXTE* data gives estimates which are very much better constrained than those made with the *ASCA* SIS data. The estimate from our *RXTE* data of $M_{WD} = 1.21$ (1.16-1.28) $M_\odot$ corresponds well to that of 1.21 (> 1.08)$M_\odot$ obtained with *Ginga* data. Although this appears to be unusually high Ramsay (2000) found that the white dwarf in magnetic CVs were biased towards higher masses compared to isolated white dwarfs.

ACKNOWLEDGEMENTS

We gratefully acknowledge Darragh O'Donoghue for the use of his period analysis software and also the referee, Chris Done, for her helpful comments.

REFERENCES

Allan, A., Hellier, C., Beardmore, A., 1998, MNRAS, 295, 167

Allan, A., Horne, K., Hellier, C., Mukai, K., Barwig, H., Bennie, P.J., Hilditch, R.W., 1996, MNRAS, 279, 1345.
Cropper, M., Ramsay, G., Wu, K., 1998, MNRAS, 293,222
Cropper, M., Wu, K., Ramsay, G., Kocabiyik, A., 1999, MNRAS, 306, 684
Deeming, T.J., 1975, Ap & SS, 36, 137
Duck, S.R., Rosen, S.R., Ponman, T.J., Norton, A.J., Watson, M.G. and Mason, K.O., 1994, MNRAS, 271, 372
Fujimoto, R., Ishida, M., 1996, ApJ, 474, 774
Frank, J., King, A., Raine, D., 1992, Accretion Power in Astrophysics, Cambridge University Press, Cambridge.
Ghosh, P., Lamb, F., 1978, ApJ, 223, L83.
Hellier, C., Ramseyer, T., Jablonski, F.J., 1994, MNRAS, 271, L25
James, C.H., 2001, MPhil Thesis, University of London.
James, C.H., Branduardi-Raymont, G., Cropper, M., Ramsay, G., 1998, in Proceedings of the First XMM Workshop, "Science with XMM", held at Noordwijk in the Netherlands, Dahlem, M. (ed.), URL http://astro.estec.esa.nl/
King, A.R., Shaviv, G., 1984, MNRAS, 211, 883.
Kurtz, D.W, 1985, MNRAS, 213, 773
Li, J., Wickramasinghe, D.T & Rudiger, G., 1996, ApJ, 469, 765
Mason, K.O., 1997, MNRAS, 285, 493
Mason, K.O., Watson, M.G., Ponman, T.J., Charles, P.A., Duck, S.R., Hassall, B.J.M., Howell, S.B., Ishida, M., Jones, D.H.P., Mittaz, J.P.D., 1992, MNRAS, 258, 749
Mewe R., Kaastra J.S., Liedahl D.A., 1995, Legacy, 6, 16
Nauenberg, M., 1972, ApJ, 175, 417.
Norton, A. J., Beardmore, A. P., Allan, A., Hellier, C., 1999, A&A, 347, 203
Patterson, J., 1994, PASP, 106, 209
Piirola, V., Hakala, P., Coyne, G.V., 1993, ApJ, 410, L107
Plavec, M., & Kratochvil, P. 1964, BAIC, 15, 165
Potter, S. B., Cropper, M.,Mason, K. O., Hough, J. H. and Bailey, J. A., 1997, MNRAS, 285, 82
Ramsay, G., 2000, MNRAS, 314, 403.
Ramsay, G., Cropper, M.S., Hellier, C., Wu, K., 1998, MNRAS 297, 1269
Rosen, S.R., 1992, MNRAS, 254, 493
Rosen, S.R., Mason, K. O., Cordova, F. A., 1988, 231, 549.
Rosen, S.R., Mittaz, J.P.D., Hakala, P.J., 1993, MNRAS, 264, 171
Scargle, J.D., 1982, ApJ, 263, 835.
Swank, J.H, 1998, The Active X-Ray Sky: Results from BepposAX and RXTE. Proceedings of the Active X-ray Sky symposium, 21–24 October, 1997, Rome, Italy, Edited by L. Scarsi, H. Bradt, P. Giommi, and F. Fiore. Publisher: Amsterdam: Elsevier, 1998.
Tanaka, Y., Inoue, H., Holt, S.S., 1994, PASJ, 46, L37
Väth, H., Chanmugam, G., & Frank, J., 1996, ApJ, 457, 407
Warner, B., 1995, in Cataclysmic Variables, Cambridge University Press, Cambridge.
Wickramasinghe, D.T., 1988, Polarized Radiation of Cirmstellar Origin, eds Coyne, G.V. et al. Obs., Vatican, Vatican. p. 1.
Wu, K., Chanmugam, G., & Shaviv, G., 1995, ApJ, 455, 260.
Yaqoob, T., ASCATEAM, 2000, ASCA GOF Calibration Memo, ASCA-CAL-00-06-01, v1.0 (06/05/00).